Angular Distribution Models, Anisotropic Correction Factors, and Mixed Clear-Scene Types: A Sensitivity Study

Cédric Bertrand, Nicolas Clerbaux, Alessandro Ipe, Steven Dewitte, and Luis Gonzalez

***Abstract*—Because radiometers do not measure the earth's outgoing flux directly, angular distribution models (ADMs) are used to invert measured radiances at the top of atmosphere (TOA) to flux. However, data used to build ADMs are generally not sorted for mixed scene types, and anisotropic correction factors for such scenes are not usually available. In the present study, we have analyzed shortwave (SW) flux values retrieved over nine areas representative of a junction between two different ADM scene types in the Meteosat-7 field of view. The Clouds and the Earth's Radiant Energy System (CERES) broadband SW ADMs were used to perform the radiance-to-flux conversion. Because of the large anisotropy difference that can exist between ADMs, use of the ADM that corresponds to the scene type with the highest percent coverage over footprints containing a mixture of scene types generates instantaneous as well as systematic errors in the retrieved SW flux values. Nevertheless, in the absence of available mixed scene type ADMs, we show that the CERES on the Tropical Rainfall Measuring Mission satellite SW ADMs can be combined together to provide reliable mixed scene types anisotropic correction factors. The use of such anisotropic factors appears to be especially well suited along the coastline of continents.**

***Index Terms*—Anisotropic correction, remote sensing, sea ice, solar radiation, vegetation.**

I. Introduction

THE DETERMINATION of the earth's radiation budget (ERB), which represents the balance between incoming energy from the sun and outgoing thermal [longwave (LW)] and reflected [shortwave (SW)] energy from the earth, is essential to atmospheric modeling and climate studies. Satellites ERB data are fundamental for the development of realistic climate models and the study of natural and anthropogenic perturbations of the climate [1]. However, spaceborne radiometers cannot measure the earth outgoing SW and LW flux directly. Rather, they can only instantaneously measure the radiance in a single viewing direction. Flux (F) is related to radiance (L) as follows:

$$F(\theta_s) = \int_0^{2\pi} \int_0^{\pi/2} L(\theta_s, \theta_v, \phi) \cos\theta_v \sin\theta_v d\theta_v d\phi$$

where θ_s is the solar zenith angle, θ_v the observer viewing zenith angle, and ϕ the relative azimuth angle defining the azimuth angle position of the observer relative to the solar plane. Analysis of satellite measurements for ERB determination requires information about the angular characteristics of radiation that is reflected (SW) and emitted (LW) from the earth–atmosphere system [2]. These angular characteristics can be defined by models that express, for an imaginary surface element at the top of the atmosphere (TOA), the outgoing radiance intensity as a function of the total hemispheric flux leaving the element [3]. In principle, a radiance measurement at a single angle can then be converted into an inferred hemispheric flux. For successful application of the angular distribution models (ADMs), it is necessary to classify the earth observations into a set of scenes (e.g., ocean, land, snow, and clouds) and to have a complete set of angular models for each scene class because ADMs, to a large extent, determine the accuracy of the derived radiation budget.

Past investigations of the ERB from satellite measurements have varied considerably in the approach to angular models for reflected radiation. As an example, to analyze the Nimbus 3 measurements, Raschke *et al.* [4] used three scenes (ocean, snow, and a cloud–land combination) and "gross-empirical" models derived from a variety of sources including aircraft, balloons, and early satellite data. Because of the lack of well-defined ADMs, Gruber [5] assumed isotropy for all SW observations while analyzing the National Oceanic and Atmospheric Administration (NOAA) scanning radiometer data. For the Nimbus 7 ERB measurements, Jacobowitz *et al.* [6] used four scenes (ocean, land, snow–ice combination, and cloud). Based on Nimbus-7 ERB scanner radiance measurement sorted by angular bins [7], Suttles *et al.* [3], [8] derived 12 ADM scene types (hereafter referred as ERBE ADMs) stratified by surface type (ocean, land, snow, desert, and land–ocean mix) and four approximate cloud cover classes (clear, partly cloudy, mostly cloudy, and overcast). These ADMs have been used in the Earth Radiation Budget Experiment (ERBE) [9] inversion algorithm [10] in order to infer hemispheric flux from ERBE radiance [2], [11].

More recently, using an approach similar to that used by Suttles *et al.* [3], [8], Loeb *et al.* [12] derived from radiance measurements performed by the Clouds and Earth's Radiant Energy System (CERES) instruments [13] onboard the Tropical Rainfall Measuring Mission (TRMM) satellite [14] a far greater number of ADM scene types ($\approx$200 SW and several hundred LW ADM scene types) (hereafter referred as CERES–TRMM

Manuscript received March 16, 2004; revised August 20, 2004. This work was supported by the "Prodex Program" under PRODEX-7 Contract 15162/01/NL/SFe (IC), Belgian State, Prime Minister's Office, Federal Office for Scientific, Technical and Cultural Affairs.

The authors are with the Department of Observations, Section Remote Sensing from Space, Royal Meteorological Institute of Belgium, B-1180 Brussels, Belgium (e-mail: Cedric.Bertrand@oma.be).

Digital Object Identifier 10.1109/TGRS.2004.838361

ADMs). For clear scenes, CERES–TRMM ADMs are defined over ocean, land, and desert, while theoretical ADMs are used over snow. Over clear ocean, ADMs are wind speed dependent and use a theoretical adjustment to account for aerosol optical depth variations. Over vegetation, ADMs are divided into two classes: low to moderate tree/shrub coverage and moderate to high tree/shrub coverage. Desert ADMs are defined for dark and bright desert regions. ADMs for cloudy conditions are defined for several classes stratified by surface type, cloud fraction, cloud phase, and cloud optical depth.

CERES–TRMM ADMs undoubtedly represent a major advance over previous ADMs regarding the large number of scene types but also in terms of angular resolution. The relative azimuth angle (ϕ) range from 0° to 180° (models are assumed to be azimuthally symmetric about the principal plane) and ten angular bins are considered (with a 10° or 20° step). Angular bins for the sun zenith angle (θ_s) are defined over the same intervals as for the satellite zenith angle (θ_v) (i.e., nine angular bins from 0° to 90° in 10° step). In comparison, ERBE ADMs were calculated as a function of ten solar zenith angles, seven viewing zenith angles, and, eight relative azimuth angles.

However, while ERBE SW ADMs account for a land–ocean mix surface type, no mixed surface scene types have been derived when building the CERES–TRMM SW ADMs. However, previous studies (e.g., [12] and [15]) have demonstrated that changes in the physical and optical properties of a scene have a strong influence on the anisotropy of the radiation at the TOA. The anisotropy of surface-leaving radiance depends on several factors, including vegetation coverage, surface type, and surface heterogeneity [16]. Therefore, ignoring these effects by applying pure scene type ADMs when performing the radiance-to-flux conversion (e.g., using the ADM that corresponds to the scene type with the highest percent coverage over the footprint) could result in flux errors over footprints containing a mixture of scene types.

Being involved in the Geostationary Earth Radiation Budget (GERB) radiometer [17] ground segment, we have investigated if the highest percent coverage ADM scene type approach does not lead to instantaneous and systematic errors in retrieved SW flux at the TOA when radiance measurements originate from footprints containing a mixture of scene types. The GERB ground segment aims to deliver nearly real-time estimates of the radiation budget for the region covered by Meteosat Second Generation (MSG-1) [18] at the 3×3 Spinning Enhanced Visible and Infra Red Imager (SEVIRI) pixels resolution. The resolution enhancement is obtained by merging data streams from the two instruments (the GERB spatial resolution is about 50 km at nadir, and the SEVIRI resolution is 3 km at the satellite subpoint). Therefore, in the absence of reliable GERB data at the present time (while MSG-1 commenced routine operations on January 29, 2004, the GERB data are still in validation phase), we have considered clear-sky SW flux retrieved from Meteosat-7 (MS-7) data using the CERES–TRMM SW ADMs (on TRMM, CERES has a spatial resolution of approximately 10 km) to perform the SW radiance-to-flux conversion (on a 3×3 MS-7 pixel resolution) as surrogate for the GERB SW flux at the 3×3 SEVIRI pixels resolution.

While several years of CERES–Terra data have provided enough sampling to define new ADMs at a significantly higher angular resolution than allowed by TRMM data, we have only considered the CERES–TRMM SW ADMs in the present study. The reason is that CERES–TRMM SW ADMs are more relevant to process geostationary data. The TRMM spacecraft is in a 350-km circular, precessing orbit with a 35° inclination angle. This orbit samples each grid box in the tropics and subtropics about once per day, but at different local time every day. Because TRMM has a 46-day repeat cycle, the full range of solar zenith angle is acquired over a region every 46 days (each grid box is sampled three times for each hour of the day within a single season). On the other hand, while CERES on the Terra (and Aqua) spacecraft greatly extends the CERES–TRMM data by adding midlatitude and polar observations, they are on a polar sun-synchronous orbit designed to cross the equator at approximately the same local time each orbit. Therefore, CERES–Terra (and CERES–Aqua) data does not allow to provide observations of the angular radiation fields of some CERES scene types over the full range of solar zenith angles. Consequently, the new set of global CERES ADMs based on two years of CERES–Terra measurements (as the forthcoming CERES–Aqua ADMs) has empty ADMs angular bins (N. Loeb, personal communication, March 2004). Because geostationary data exhibits the full range of solar zenith angle, scene-dependent empirical ADMs built from CERES–TRMM measurements are, therefore, more suitable to convert GERB SW radiance into reflected SW flux at TOA even if TRMM data were restricted to roughly cover 40°S to 40°N. In addition, on TRMM, CERES has a spatial resolution of approximately 10 km (equivalent diameter), which is closer to the 3×3 SEVIRI pixels resolution than the 20 km of CERES resolution on Terra. And finally, by contrast to the TRMM CERES measurements, CERES flux retrievals for the Terra satellite do consider mixed-scene pixels at the boundaries between land and ocean and between snowy and snow-free areas.

The paper is subdivided as follows. First, we describe how the outgoing clear-sky SW radiative flux are retrieved from MS-7 data. Second, we compare and discuss SW flux resulting from a radiance-to-flux conversion performed on the basis of the highest percent coverage ADM scene type approach and flux resulting from the use of mixed scene types anisotropy correction factors. The latter are derived from the combination of the existing CERES–TRMM broadband SW ADMs. Finally, we conclude.

II. Reflected TOA Clear-Sky SW Flux Computation

MS-7 like other imaging radiometers of meteorological satellites is first designed to make pictures of cloud patterns, and accurate radiometric calibration of its channels are not emphasized. Infrared and water vapor channels calibrations are provided, but there is no onboard calibration device for the visible channel (only a raw estimate of the visible-channel calibration is provided by Eumetsat). To overcome this weakness, a cross calibration of the MS-7 visible channel has been performed [19] according to the well-calibrated SW channel of the CERES instrument on the TRMM and Terra spacecrafts [13].

MS-7 does not measure the total SW radiance reaching the instrument, but only the radiance in its visible channel (0.45–1.0 μm), $L_{\rm vis}$. For this reason, the total (or broadband) SW radiance ($L_{\rm sw}$) is estimated from the visible filtered measurement using a third-order regression

$$L_{\rm sw} = D_0(\theta_s) + D_1(\theta_s)L_{\rm vis} + D_2(\theta_s)L_{\rm vis}^2 + D_3(\theta_s)L_{\rm vis}^3 \quad (1)$$

where the regression coefficients $D_i (i = 0, \ldots, 3)$, which depend on the solar zenith angle (θ_s), are obtained by least mean square minimization on a database of spectral radiance curves. It is worth pointing out that in (1), the narrowband-to-broadband (NB-to-BB) conversion coefficients are neither dependent on the viewing zenith angle nor on the azimuth angle because the radiative transfer model used to generate the spectral radiance database supposes Lambertian surface reflectance.

By contrast to the NB-to-BB SW radiance conversion, our BB radiance-to-flux conversion accounts for the nonisotropic distribution of the radiance. Because most natural surfaces are non-Lambertian, we make use of the CERES–TRMM SW ADMs [13] to perform the angular integration. Considering the appropriate CERES–TRMM ADM scene type, the instantaneous broadband SW flux F is computed from the directional SW broadband radiance by using

$$F(\theta_s) = \frac{\pi L(\theta_s, \theta_v, \phi)}{R(\theta_s, \theta_v, \phi)} \quad (2)$$

where R, the ADM-dependent anisotropic correction factor (ACF) for a given scene type and viewing geometry, is the ratio between the assumed Lambertian flux to the real flux [3]. The ADM ACFs for a given scene type j are given by [15]

$$R_j(\theta_{si}, \theta_{vk}, \phi_l) = \frac{\pi \bar{L}_j(\theta_{si}, \theta_{vk}, \phi_l)}{F_j(\theta_{si})}$$

where $\bar{L}_j(\theta_{si}, \theta_{vk}, \phi_l)$ is the mean outgoing broadband radiance at TOA (corrected for the earth–sun distance) for a given interval of solar zenith angle θ_{si}, viewing zenith angle θ_{vk}, and relative azimuth angle ϕ_l; $F_j(\theta_{si})$ is the corresponding flux determined by integration of $\bar{L}_j(\theta_{si}, \theta_{vk}, \phi_l)$ over all up-welling directions.

The conversion of one MS-7 footprint BB radiance into the corresponding flux requires therefore a scene identification to properly select the adequate SW ADM among the CERES–TRMM SW ADMs. This needs the characterization of the surface type within the footprint. In practice, the Global Land Cover Map (version v1.2) produced by the International Geosphere Biosphere Program (IGBP, [20], [21]) is used to associate one of the six CERES–TRMM class to each MS-7 pixels. This was done by merging the 17 IGBP surface types into the 6 CERES–TRMM surface types (see Table I and Fig. 1). As the IGBP map does not allow accurate discrimination between bright and dark desert, an additional desert footprint registration is performed using the "CERES IGBP map" (CERES uses a 10′ latitude by 10′ longitude map of IGBP types that covers the globe. See [12] for further information). It is worth pointing out that except for ice/snow, the MS-7 pixel registration according to the CERES–TRMM classes is taken invariant in time. Obviously this can potentially introduce some limitations in our flux retrieval accuracy but is justified in the sense that CERES–TRMM ADMs have been derived using an invariant surface type map (except for snow) and have to be viewed for a given class as representative of the mean state/behavior of this particular class. As we have only considered clear-sky SW flux in this study, we do not extend here on the

TABLE I
IGBP LAND COVER LEGEND AND ASSOCIATED CERES–TRMM SCENE TYPES

IGBP type	CERES-TRMM surface type
1. Evergreen Needle-leaf Forest	mod-to-high Tree/Shrub cover.
2. Evergreen Broadleaf Forest	mod-to-high Tree/Shrub cover.
3. Deciduous Needle-leaf Forest	mod-to-high Tree/Shrub cover.
4. Deciduous Broadleaf Forest	mod-to-high Tree/Shrub cover.
5. Mixed Forest	mod-to-high Tree/Shrub cover.
6. Closed Shrub-lands	mod-to-high Tree/Shrub cover.
7. Open Shrub-lands	dark desert
8. Woody Savannas	mod-to-high Tree/Shrub cover.
9. Savannas	low-to-mod Tree/Shrub cover.
10. Grasslands	low-to-mod Tree/Shrub cover.
11. Permanent Wetlands	mod-to-high Tree/Shrub cover.
12. Croplands	low-to-mod Tree/Shrub cover.
13. Urban and Built-Up	dark desert
14. Cropland/Natural Vegetation Mosaic	low-to-mod Tree/Shrub cover.
15. Snow and Ice	snow
16. Barren or Sparsely Vegetated	bright desert
17. Water Bodies	ocean
99. Interrupted Areas	-
100. Missing Data	-

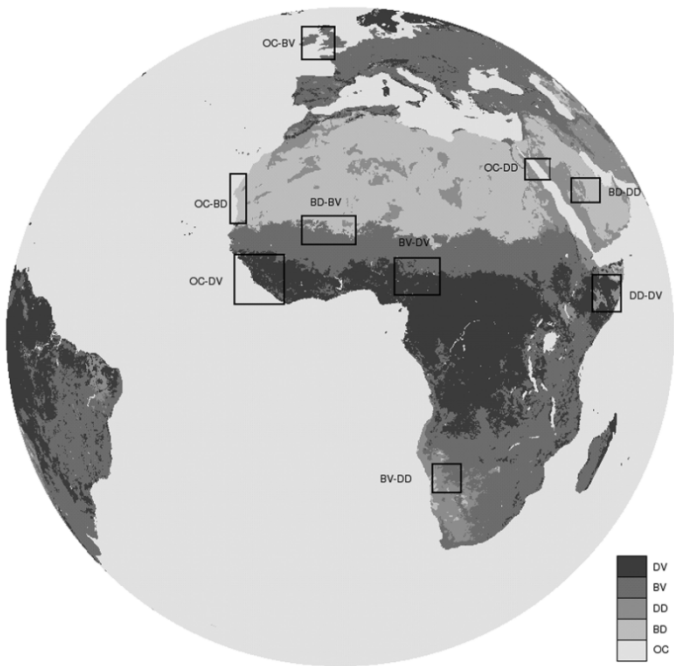

Fig. 1. CERES ADMs surface geotypes as seen by Meteosat-7 imager (OC = ocean, DV = moderate to high vegetation cover, BV = low to moderate vegetation cover, DD = dark desert, and BD = bright desert). Boxes delimit the nine areas we selected in the Meteosat-7 field of view as representative of junction between two CERES–TRMM ADMs scene types.

cloud property retrieval needed to properly select SW cloudy ADMs. Nevertheless, reader can found further information on our cloud-screening algorithm in [22] and [23].

The anisotropy of the earth's scenes generally varies with viewing geometry and cloud/clear-sky properties in a continuous manner. However, CERES ADMs are defined for discrete angular bins and scene. Therefore, the CERES ACFs have to be adjusted to avoid introducing large instantaneous flux errors or sharp flux discontinuities between angular bins or scene types. To reduce angular bin discretization errors, we estimate ACFs by linearly interpolating bin-averaged ACFs to each observation angle $(\theta_s, \theta_v, \phi)$ (in the SW, the ACF is a function of all three angles). The ADM ACF $[R_j(\theta_{si}, \theta_{vk}, \phi_l)]$ for a given scene type (j) in a given angular bin $(\theta_{si}, \theta_{vk}, \phi_l)$ is assumed to correspond to the midpoint of the discrete angular bin defined by $(\theta_{si} \pm (\Delta\theta_s)/(2), \theta_{vk} \pm (\Delta\theta_v)/(2), \phi_l \pm (\Delta\phi)/(2))$, where $\Delta\theta_s, \Delta\theta_v, \Delta\phi$ represent the angular bin resolutions. The estimation of the ACF for the set of observation angles $(\theta_s, \theta_v, \phi)$ is then performed by a three-dimensional linear interpolation.

III. Study Areas Definition and Selected MS-7 Data

Nine areas have been selected in the MS-7 field of view (FOV) to investigate the impact of the ADM ACF on the SW flux values (see Fig. 1). Each area is representative of a junction between two CERES scene types. The following scene types have been considered: ocean surface, moderate to high tree/shrub coverage (dark vegetation surface), low to moderate tree/shrub coverage (bright vegetation surface), bright desert surface, and dark desert surface. The nine scene type combinations we considered are: (A) ocean and bright vegetation (OC-BV), (B) ocean and dark vegetation (OC-DV), (C) ocean and bright desert (OC-BD), (D) ocean and dark desert (OC-DD), (E) bright desert and dark desert (BD-DD), (F) bright desert and bright vegetation (BD-BV), (G) bright vegetation and dark vegetation (BV-DV), (H) bright vegetation and dark desert (BV-DD), and (I) dark desert and dark vegetation (DD-DV), respectively. Note that the BD-DV combination does not occur in the MS-7 FOV. It is worth pointing out that the snow and ice surface types were not considered here and that the clear ocean ADM was taken as being the "all wind speed" ADM. Locations of these areas in the MS-7 FOV have been determined in order to account for the presence of footprints in which the fraction of each considered scene varies continuously from 0% to 100%. Their sizes (geographical extent) were chosen to be as small as possible in order to have a large homogeneity in the surface types as well as in the footprints acquisition geometry (e.g., in the θ_s, θ_v, and ϕ angles).

In each area, we have analyzed all available 12:00 UTC MS-7 time slot during February 2003. The day exhibiting the largest number of clear-sky footprints was selected. Then, clear-sky footprints were gathered by discrete bins of 10% in surface types coverage. Solid lines in Fig. 2 display for each area the resulting bin-averaged SW radiance values (date of the corresponding selected day is supplied in the subfigures title).

Fig. 2 indicates that in some areas the bin-averaged SW radiances do not behave linearly when moving from a 100% surface coverage of type 1 to a 100% surface coverage of type 2 [e.g., see the bin-averaged OC-BD SW radiances in Fig. 2(C)]. Because such nonlinear transitions question the assumption of surface coverage homogeneity throughout a given scene type in the selected areas, we have also considered more idealized situations. For these idealized cases, SW radiance values were obtained by

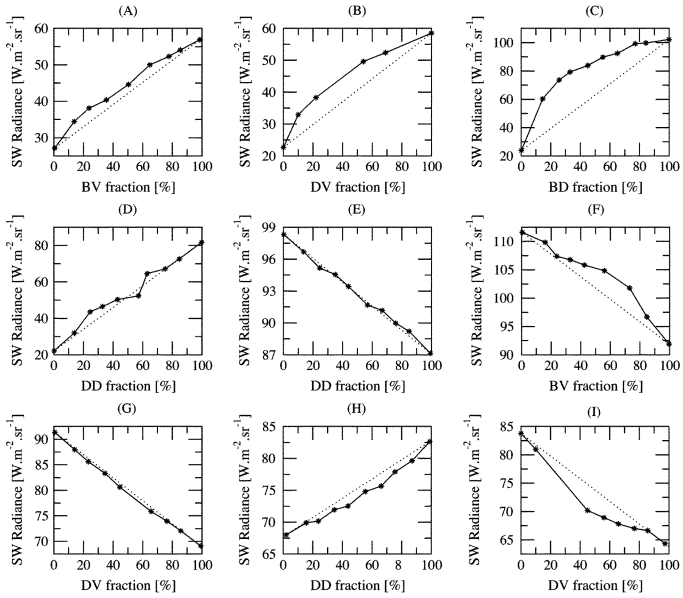

Fig. 2. (Solid lines) Bin-averaged and (dotted lines) idealized clear-sky TOA SW radiances. The following scene types combination are considered: (A) ocean and bright vegetation (OC-BV) [02.15.03], (B) ocean and dark vegetation (OC-DV) [02.24.03], (C) ocean and bright desert (OC-BD) [02.06.03], (D) ocean and dark desert (OC-DD) [02.27.03], (E) bright desert and dark desert (BD-DD) [02.26.03], (F) bright desert and bright vegetation (BD-BV) [02.15.03], (G) bright vegetation and dark vegetation (BV-DV) [02.20.03], (H) bright vegetation and dark desert (BV-DD) [02.02.03], and (I) dark desert and dark vegetation (DD-DV) [02.03.03]. Date in brackets informs about the day of the selected 12:00 UTC MS-7 time slot in each area (defined in Fig. 1).

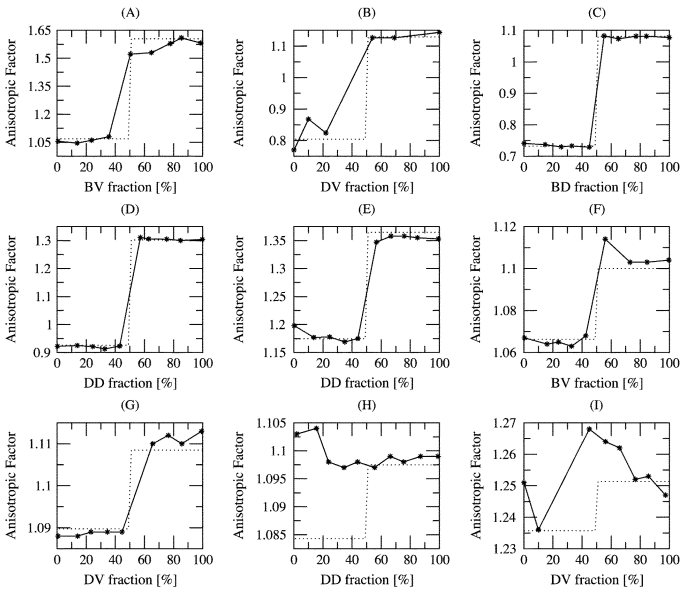

Fig. 3. (Solid lines) Bin-averaged and (dotted lines) area-averaged anisotropic correction factors computed according to the CERES–TRMM SW ADMs that correspond to the scene type with the highest percent coverage within the footprints. For each area (defined in Fig. 1), the same scene type combination and day as in Fig. 2 is considered.

TABLE II
AVERAGED CLEAR-SKY FOOTPRINTS ACQUISITION ANGLES (SOLAR ZENITH ANGLE θ_s, VIEWING ZENITH ANGLE θ_v, AND RELATIVE AZIMUTH ANGLE ϕ) FOR EACH STUDY AREA DEFINED IN FIG. 1. ALSO PROVIDED ARE THE ADM ACFS (ΔR) AND THE INSTANTANEOUS REFLECTED SW TOA FLUX (ΔF) DIFFERENCES AT THE SHIFTING POINT (RELATIVE DIFFERENCE GIVEN IN PERCENT) BETWEEN ADMS SCENE TYPES. THE FOLLOWING SCENE TYPES ARE CONSIDERED: OC = OCEAN SURFACE, BV = BRIGHT VEGETATION SURFACE (LOW TO MODERATE TREE/SHRUB COVERAGE), DV = DARK VEGETATION SURFACE (MODERATE TO HIGH TREE/SHRUB COVERAGE), BD = BRIGHT DESERT SURFACE, AND DD = DARK DESERT SURFACE TYPES

Scene types	$\bar{\theta_s}$ (degree)	$\bar{\theta_v}$ (degree)	$\bar{\phi}$ (degree)	ΔR	Δ F (W.m^{-2})
OC-BV	66.70	61.14	175.21	0.54 (50.1%)	39.84 (32.4%)
OC-DV	23.87	14.36	168.95	0.32 (40.3%)	43.12 (27.5%)
OC-BD	42.84	30.69	173.97	0.35 (47.5%)	81.26 (30.5%)
OC-DD	44.89	49.82	165.26	0.38 (40.8%)	47.49 (27.3%)
BD-DD	48.62	55.65	165.54	0.19 (16.2%)	35.06 (14.1%)
BD-BV	29.53	18.68	167.99	0.03 (3.2%)	10.34 (3.4%)
BV-DV	21.22	16.44	142.59	0.02 (1.7%)	05.19 (2.2%)
BV-DD	08.51	30.39	166.71	0.01 (1.2%)	01.75 (0.8%)
DD-DV	43.00	52.00	154.00	0.02 (1.3%)	03.35 (1.8%)

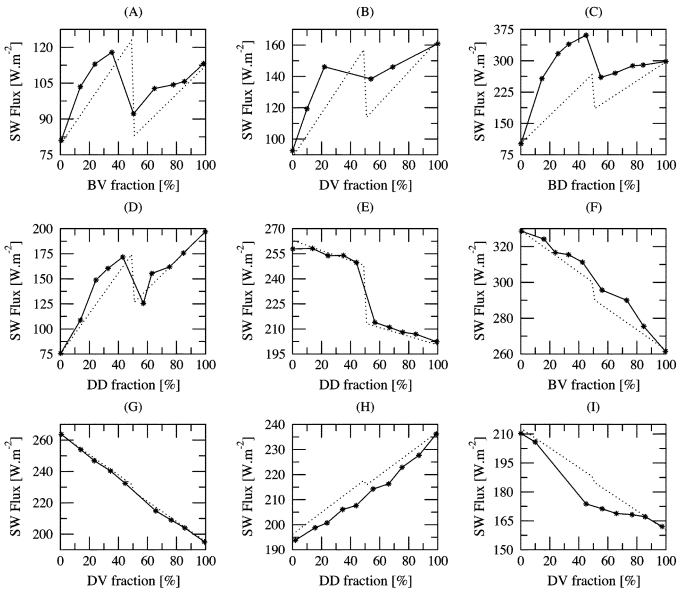

Fig. 4. (Solid lines) Bin-averaged and (dotted lines) idealized reflected SW flux at TOA computed according to the highest percent coverage ADM scene type approach. For each area (defined in Fig. 1), the same scene type combination and day as in Fig. 2 is considered.

simple linear interpolation between the averaged clear SW radiance values originating from footprints 100% covered by a scene of type 1 and 2, respectively (see dotted lines in Fig. 2).

IV. CERES–TRMM ADM ACFs

For each area, the solid line in Fig. 3 displays the bin-averaged CERES–TRMM ADM ACF corresponding to the CERES scene exhibiting the highest percent coverage within the footprints. Because any angular acquisition characteristics (e.g., θ_s, θ_v, and ϕ) are directly related to idealized SW radiance values (dotted lines in Fig. 2) idealized ACFs cannot be retrieved from the CERES–TRMM ADMs. To overcome such a difficulty, averaged $\bar{\theta_s}, \bar{\theta_v}$, and $\bar{\phi}$ values computed from θ_s, θ_v, and ϕ of all clear-sky footprints found in each area were considered. The averaged acquisition angles are given in Table II for each study area. In the following parts of this paper, we will refer to the "bin-averaged" ACFs (mean value of all footprints ACF found in a given coverage bin) and to the "area-averaged" ACFs (ACF determined by considering the averaged values of the three acquisition angles of each footprints found inside the full area). The bin-averaged ACF is, thus, bin-dependent by contrast to the area-averaged ACF, which is bin-invariant. More specifically, its value is constant for each of the two ADM scene types found in an area as illustrated by the dotted lines in Fig. 3.

Analysis of the ACF values given in Fig. 3 reveals that globally the footprints acquisition geometry do not vary too much from one coverage bin to another inside a given area. However, some discrete coverage bins appear to be not homogeneously distributed in some areas. As an example, Fig. 3(A) indicates some discrepancies between the bin- and area-averaged ACFs (solid versus dotted lines) in the 50% to 60% and 60% to 70% coverage bins.

Nevertheless, whatever the variations in the footprints acquisition angles may be, the ACF values displayed in Fig. 3 clearly indicate that the largest surface anisotropy variations between clear CERES–TRMM scene types occur along the coastline of continents [Fig. 3(A)–(D)]. The relative difference in ACFs can reach up to about 50% between the oceanic and the vegetation or desert scene types (see Table II). While of lower magnitude, Fig. 3(E) reveals that difference in the ADMs ACFs between the two desert surfaces can reach up to 16%; the BD surface being more isotropic, presumably due to the lower vegetation coverage there. By contrast, the difference in the ACFs between the two vegetation surfaces is only 1.7%, with BV being slightly more isotropic than DV [see Fig. 3(G)]. More surprising are the reduced ACF differences between the dark desert and the vegetation surfaces in Fig. 3(I) and (H). Indeed, while the difference between the BD-DV scene types ACFs accounts for 3.2% [see Fig. 3(F)], the differences reduce to 1.2% between the BV-DD [Fig. 3(H)] and to 1.3% between the DD-DV [Fig. 3(I)] scene types, respectively. Such limited differences between these scene types explain why the bin-averaged ACF values do not satisfactorily cope with the corresponding area-averaged ADMs values over these two junctions. Indeed, variations in the ADM ACFs due to angular change in the footprints acquisition geometry are larger than the anisotropy difference between the two scene types that are present. Note that [12] estimated the variability in the ACF to be <0.04 and <0.03 at the 95% confidence level for most solar zenith and viewing zenith angle bins for vegetation surface types (BV and DV) and desert surface types (BD and DD), respectively.

Fig. 4 and Table II clearly indicate that using the ADM ACFs, which correspond to the dominant scene type over a mixed footprint when performing the radiance-to-flux conversion, leads to generate an artificial flux discontinuity at the shifting point between the two ADMs scene types. As an example, moving from the clear OC ADM to the BV ADM results in an instantaneous flux drop of about 32% (relative difference) or 40 W $\cdot$ m^{-2} (see the dotted line in Fig. 4(A) and Table II). Similarly, Fig. 4(C) and Table II indicate that a shift from the clear OC ADM to the

BD ADM reduce the reflected instantaneous SW flux at the TOA of about 80 W $\cdot$ m^{-2} (equivalent to a flux drop of about 30%) in the idealized case (dotted line) and a bit more (about 100 W $\cdot$ m^{-2}) for the bin-averaged flux (solid line). On the other hand, shifting from the BV ADM to the DD ADM or from the DD ADM to the DV ADM has a limited influence on the retrieved SW flux at the TOA (Table II and Fig. 4(H) and (I) only report a flux change of few percents).

As we see, ignoring the changes in the physical and optical properties of a surface leads to erroneous estimation of the reflected instantaneous SW flux at the TOA. Based on the concept of the linear mixing model, we have investigated if the existing CERES–TRMM SW ADMs could be combined together to provide reliable mixed scene types ACFs.

V. Mixed Scene Type ACFs

The linear mixing model assumes a linear relation to characterize the spectral reflectance of a mixed surface types pixel of a remotely sensed image. More specifically, under the assumption that each photon that reaches the sensor has interacted with only one surface type, the response of each pixel in each spectral band is considered as a linear combination of the responses of each component that is assumed to be in the mixture. Thus, the pixel contains information about the spectral response and the proportion of each component. The mathematical description of the linear mixing model is

$$\rho^{\text{mix}}(k) = \sum_i f_i \rho_i(k) + \epsilon(k) \tag{3}$$

where ρ^{mix} and ρ_i are the spectral reflectance of the mixed pixel and of the component i appearing in f_i percent in the mixture, in each spectral band k, respectively. $\epsilon(k)$ is the error in each sensor band k.

Considering a mixture of two components and applying the linear mixing model concept to the BB MS-7 SW radiance L, (3) can be written as follows (neglecting the error factor):

$$L^{\text{mix}} = f_1 L_1 + f_2 L_2. \tag{4}$$

Converted in terms of flux, (4) becomes

$$F^{\text{mix}} = f_1 F_1 + f_2 F_2 \tag{5}$$

where L_i is the BB radiance associated with a scene of type i appearing in f_i percent in the mixed footprint and F_i the corresponding instantaneous SW flux at the TOA (with $i = 1, 2$). Based on (2), the ACF for a mixed scene types R^{mix} is given by

$$\begin{aligned} R^{\text{mix}} &= \frac{\pi.(f_1 L_1 + f_2 L_2)}{f_1 F_1 + f_2 F_2} \\ &= \frac{f_1 \bar{R}_1 + f_2 \bar{R}_2 \cdot F_2/F_1}{f_1 + f_2 \cdot F_2/F_1} \end{aligned} \tag{6}$$

where $\bar{R}_1$ and $\bar{R}_2$ are the CERES–TRMM BB SW ADM ACFs corresponding to the CERES scene of types 1 and 2, respectively.

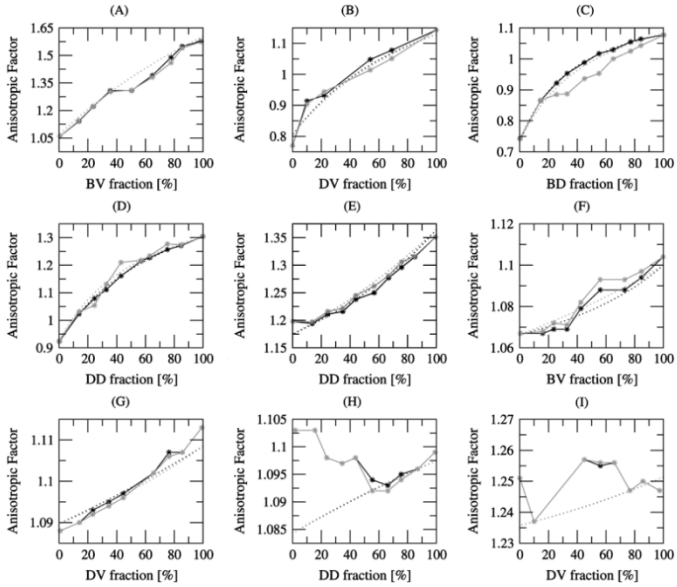

Fig. 5. (Solid lines) Bin-averaged and (dotted lines) area-averaged mixed scene types anisotropic correction factors computed according to the ADMs (in black) and to the neighboring (in gray) flux approximation, respectively. For each area (defined in Fig. 1), the same scene type combination and day as in Fig. 2 is considered.

TABLE III
Comparison Between the ADM $\bar{A}_2/\bar{A}_1$ and the Idealized $F_2^{\text{id}}/F_1^{\text{id}}$ Fluxes Ratios for Each Study Area Defined in Fig. 1. Also Provided Are the Largest Difference in the Anisotropy Correction Factor and Reflected SW Flux at the TOA Resulting From the Use of the ADM TOA Albedo Ratio Instead of the Idealized SW Flux Ratio. The Scene Types as in Table II Are Considered. Values in Brackets Are the Relative Differences in Percent

Scene types	F_2^{id}/F_1^{id}	$\bar{A}_2/\bar{A}_1$	ΔR_{max}	ΔF_{max}
OC-BV	1.42	1.39 (2.1%)	2.8E-03 (0.2%)	0.19 (0.2%)
OC-DV	1.84	1.97 (6.8%)	5.3E-03 (0.6%)	0.63 (0.5%)
OC-BD	2.93	3.56 (21.6%)	1.7E-02 (1.9%)	2.81 (1.8%)
OC-DD	2.64	2.23 (15.6%)	1.6E-02 (1.4%)	1.63 (1.4%)
BD-DD	0.76	0.64 (15.9%)	8.2E-03 (0.6%)	1.48 (0.7%)
BD-BV	0.80	0.55 (31.1%)	3.1E-03 (0.3%)	0.84 (0.3%)
BV-DV	0.74	0.87 (16.9%)	7.3E-04 (0.1%)	0.15 (0.1%)
BV-DD	1.21	1.15 (4.7%)	1.6E-04 (0.01%)	0.03 (0.01%)
DD-DV	0.75	0.77 (2.0%)	8.E-05 (6.E-03%)	0.01 (6.E-03%)

Unfortunately, (6) cannot be solved because F_1 and F_2 fluxes are unknown. A way to overcome such a limitation is to approximate the unknown F_2/F_1 ratio by the corresponding CERES–TRMM BB SW ADM flux ratio (actually by the ADM TOA albedo ratio, $\bar{A}_2/\bar{A}_1$). Adopting such an approximation, (6) reduces to

$$R^{\text{mix}} = \frac{f_1 \bar{R}_1 \bar{A}_1 + f_2 \bar{R}_2 \bar{A}_2}{f_1 \bar{A}_1 + f_2 \bar{A}_2}. \tag{7}$$

Black lines in Fig. 5 display for each selected area the mixed scene types ACFs computed according to (7). By similarity to Fig. 3, solid lines in Fig. 5 illustrate the bin-averaged and dotted lines the area-averaged mixed scene types ACFs, respectively.

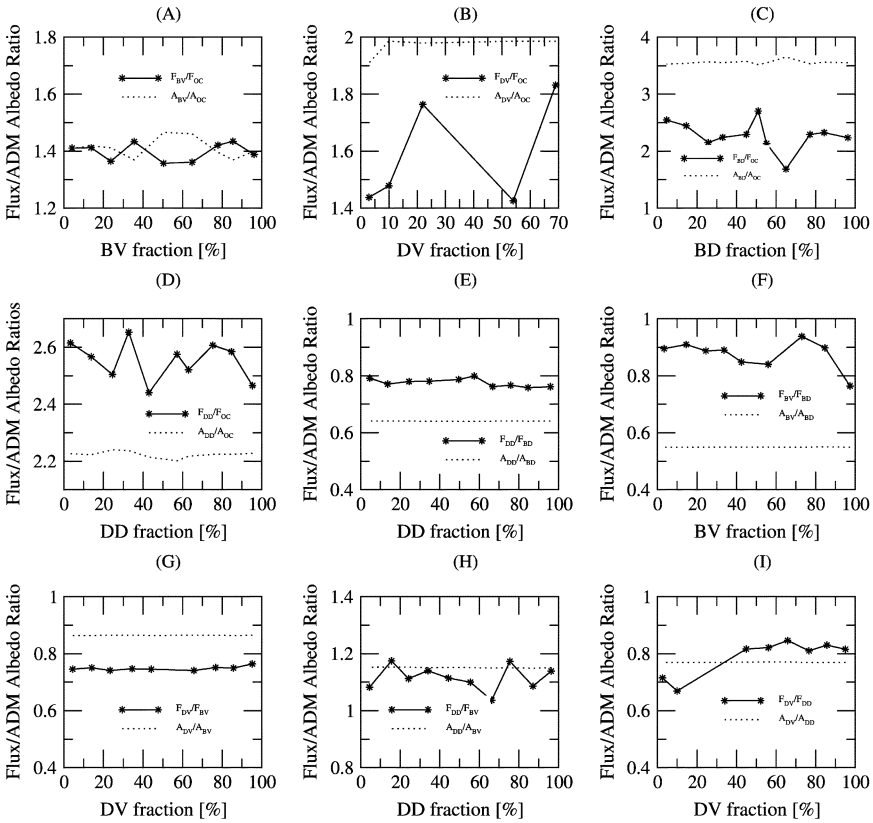

Fig. 6. Comparison between (dotted lines) the bin-averaged $\bar{A}_2/\bar{A}_1$ ADMs and (solid lines) $\bar{F}_2/\bar{F}_1$ neighboring flux ratios. For each area (defined in Fig. 1), the same scene type combination and day as in Fig. 2 is considered.

Clearly, whatever the two CERES–TRMM scene types may be, use of (7) allows a smoother transition between the two ADMs scene types. The break in the ACF values we previously reported in Fig. 3 when shifting from one ADM scene type to another does not appear anymore.

An alternative to the ADM flux (albedo) approximation is the neighboring flux approximation. It relies on the assumption that F_1 and F_2 are similar to the SW fluxes $\tilde{F}_1$ and $\tilde{F}_2$ retrieved over the geographically closest footprints in which the surface is 100% covered by a CERES scene of type 1 or 2, respectively. Gray lines in Fig. 5 display the mixed scene types ACFs for each area in Fig. 1 computed according to the neighboring flux ratio $\tilde{F}_2/\tilde{F}_1$ approach. Note that for the area-averaged mixed scene types ACFs (dotted gray lines in Fig. 5), F_1 and F_2 are known. (They are provided by the conversion of the averaged SW radiance values from footprints 100% covered by the scene of type 1 and of type 2 using the corresponding area-averaged CERES–TRMM scene types ADM ACFs.)

Table III indicates that the ADM $\bar{A}_2/\bar{A}_1$ ratio can differ up to about 31% from the corresponding idealized flux ratio $F_2^{\mathrm{id}}/F_1^{\mathrm{id}}$. Nevertheless, only a slight difference is reported (Table III) between area-averaged mixed scene types ACFs computed according to the ADM and to the neigboring flux approximation approaches, respectively (less than 2% in maximum). Similarly, the area-averaged mixed scene types ACF values displayed in Fig. 5 only reveal reduced differences between the two approaches [black versus gray dotted lines in Fig. 5(D)–(F)]. By contrast, noticeable differences between bin-averaged mixed scene types ACFs are highlighted in Fig. 5 for some coverage bins [e.g., see black versus gray lines in Fig. 5(B) and (C)]. Causes for a larger difference between the two different approximation methods in the bin-averaged values than in the area-averaged values origins in an intra/interbin(s) scene types heterogeneity throughout a given area. Because of the large number of IGBP types that can be found in a given CERES–TRMM scene type (see Table I), the surface albedo associated with a scene can vary according to the IGBP types actually found in footprints containing the scene. Therefore, the F_2/F_1 ratio computed according to the neighboring flux method (namely the $\tilde{F}_2/\tilde{F}_1$ ratio) could not be necessarily constant throughout all our discrete coverage bins in a selected area. On the other hand, the F_2/F_1 ratio estimated from ADMs (namely the $\bar{A}_2/\bar{A}_1$ ratio) is expected to be bin-invariant over a limited surface area.

Fig. 6 displays for each selected area the corresponding bin-averaged $\bar{A}_2/\bar{A}_1$ (dotted lines) and $\tilde{F}_2/\tilde{F}_1$ (solid lines) ratios, respectively. As expected, $\bar{A}_2/\bar{A}_1$ values appear to be bin-invariant over the majority of the selected areas [see Fig. 6(E)–(I)]. Nevertheless, some variations in the $\bar{A}_2/\bar{A}_1$ ratio can be observed in Fig. 6(A) and to a lesser extent in Fig. 6(C) and (D). These fluctuations originate in the nonhomogeneous distribution of some coverage bins throughout the selected area. If the majority of footprints found in a given coverage bin are preferentially located in a particular place within a given area, the averaged ADMs SW flux (albedo) ratio will differ from bin-averaged ADMs flux ratio computed over footprints well distributed into the area or located in another preferential place in the selected area. (Note that the departures we previously reported

between the bin-averaged and area-averaged ADM ACF values (black versus solid lines in Fig. 3) are another illustration of this nonhomogeneous distribution of some binned footprints throughout the selected areas.)

Regarding the bin-averaged $\tilde{F}_2/\tilde{F}_1$ ratio displayed in Fig. 6 (solid lines), values clearly vary from a discrete coverage bin to another, whatever the selected area maybe. Magnitude of the variations are larger than those reported for the $\bar{A}_2/\bar{A}_1$ ratio values. Largest departures between two successive bin-averaged $\tilde{F}_2/\tilde{F}_1$ values occur when the corresponding bin-averaged SW radiance values do not exibit a linear transition when moving from one bin to the other. As an example, Fig. 6(C) shows that the largest variations in the bin-averaged $\tilde{F}_2/\tilde{F}_1$ ratio occur at coverage bins for which the bin-averaged SW radiance values deviate from linearity when moving from 100% ocean footprints to 100% bright desert footprints [see the solid versus dotted lines in Fig. 2(C)]. On the contrary, the bin-averaged $\tilde{F}_2/\tilde{F}_1$ ratio exibits a quasi-constant value throughout the entire BD-DD and BV-DV areas as reported in Fig. 6(E) and (G), respectively. Both these areas are those for which Fig. 2 [see Fig. 2(E) and (G)] indicates a quasi-linear trend in the bin-averaged SW radiance values when moving from one CERES–TRMM scene type to another.

Also interesting to note in Fig. 6 is the difference between the corresponding bin-averaged $\tilde{F}_2/\tilde{F}_1$ and $\bar{A}_2/\bar{A}_1$ ratios values. Because CERES–TRMM ADMs are derived over several month of data, the TOA albedo may deviate from that of individual scenes used to determine the mean. Indeed, while CERES–TRMM ADMs provide information for the mean state/behavior of each scene, vegetation phenology changes from spring to spring over a 12-month cycle, which therefore impacts the associated radiance field. Moreover, even if a scene does not change, its reflectance (radiance) is allowed to vary, depending on whether it is wet or dry. Therefore, it is not at all surprising that SW flux retrieved from time-dependent radiance measurements ($\tilde{F}_1$ and $\tilde{F}_2$) can differ from the corresponding ADM mean values.

Fig. 7 presents the bin-averaged and idealized (solid versus dotted lines) reflected SW flux computed according to the ADMs and to the neighboring flux approximation methods, respectively (black versus gray lines). Differences in the idealized flux values are not apparent in the figure (see black versus gray dotted lines). As for the area-averaged mixed scene types ACFs, Table III indicates that the largest difference between the two methods accounts for less than 2% (relative difference). Such a difference appears negligible in regard to the flux discontinuity we reported in Table II (up to 32%) when estimating the idealized reflected SW flux at the TOA on the basis of the highest percent coverage ADM scene type approach.

Regarding the bin-averaged SW flux values, Fig. 7 (solid lines) clearly indicates that for a given bin the difference between flux retrieved from a radiance-to-flux conversion making use of mixed scene types ACFs (ADMs flux approximation in black and neighboring flux approximation in gray, respectively) are significantly lower than the difference existing between these fluxes and the one retrieved according to the highest percent coverage ADM scene type approach (solid lines in Fig. 4). Magnitude of the flux difference resulting from a

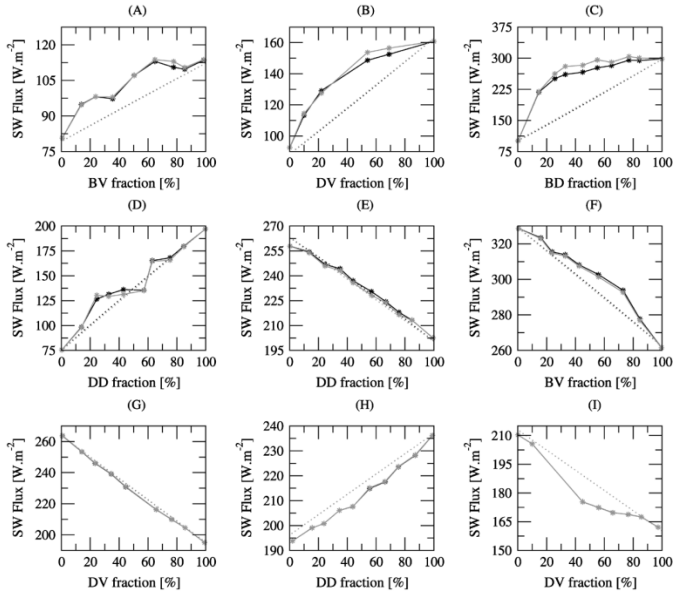

Fig. 7. Bin-averaged (solid) and area-averaged (dotted lines) reflected SW flux at TOA computed according to the ADMs (in black) and to the neighboring (in gray) flux approximation approachs, respectively. For each area (defined in Fig. 1), the same scene type combination and date as in Fig. 2 is considered.

radiance-to-flux conversion accounting for a mixed scene types ACF and, on the other hand, according to the ADM ACF of the scene with the largest percent coverage in the footprint mainly relies on the surface anisotropy difference existing between the CERES scenes contained in the footprint. As an example, larger flux differences are reported over coastal areas [compare Fig. 4(A)–(D) with Fig. 7(A)–(D)] than for junction areas between vegetation and/or desert scene types [compare Fig. 4(E)–(H) with Fig. 7(E)–(H)]. Similarly, Fig. 8 indicates that the magnitude of the flux difference resulting from the ADMs instead of the neighboring flux approximations in the mixed scene type ACF computation is also governed by the surface anisotropy difference existing between the CERES scenes contained in the footprint. We can see in this figure that a variation of $\pm 25\%$ (relative variation) in the CERES–TRMM ADMs TOA albedo will differently impact on the mixed scene types ACFs and the reflected SW flux values according to the CERES scene types in the present. A change of about 3%, 1%, and 0.12% is reported for the OC-BV, BD-DD, and BV-DV scene type combinations, respectively.

Until now, we entirely focused on instantaneous flux errors because we are mainly concerned with those in the framework of our nearly real-time estimates of the radiation budget for the regions covered by MSG-1. Nevertheless, some readers could be interested by a quantitative discussion on systematic errors (most researchers use CERES data statistically). Therefore, we have averaged, in each selected area, SW flux values retrieved over clear mixed scene type footprints. Table IV presents the differences between the averaged SW flux computed according to the highest percent coverage ADM scene type and to the mixed scene types ACF methods: $\bar{F} - \bar{F}_{\bar{A}_2/\bar{A}_1}$ and $\bar{F} - \bar{F}_{\tilde{F}_2/\tilde{F}_1}$, respectively. For each area, Table IV provides the flux differences computed from the 12:00 UTC MS-7 time slots on a daily (selected day) and monthly mean basis (February and July 2003,

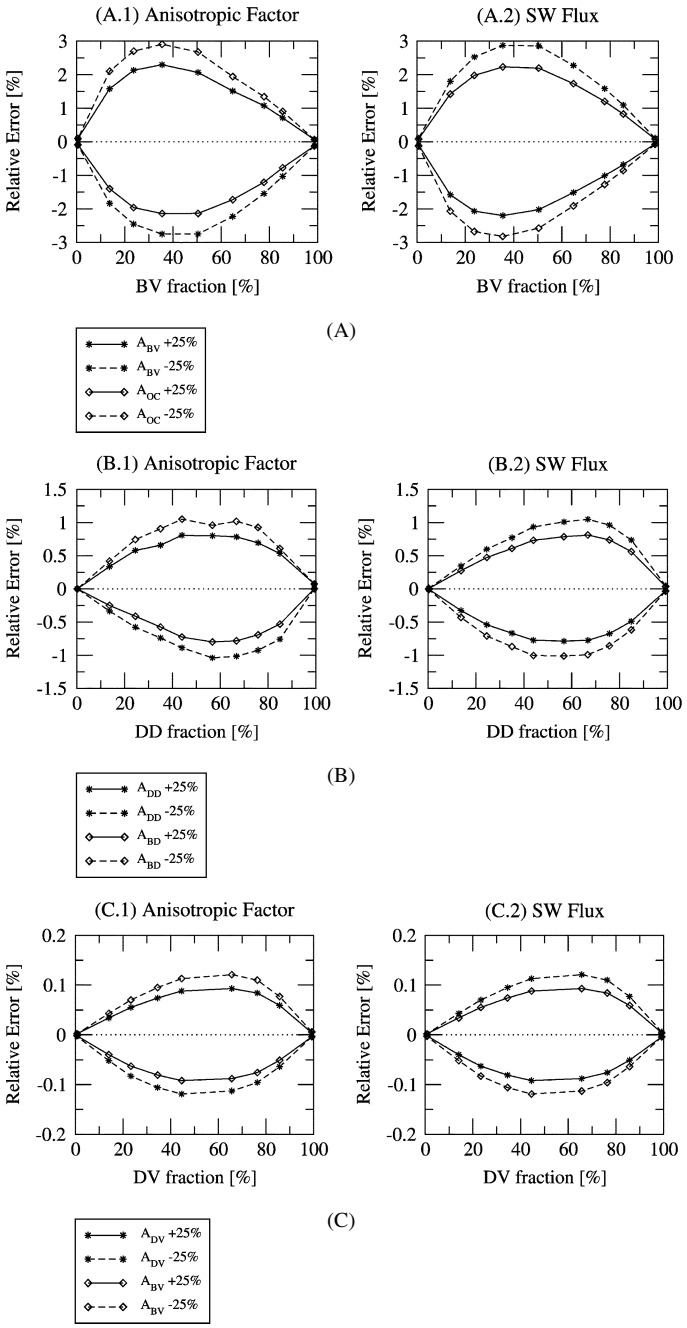

Fig. 8. Relative differences (in percent) in the bin-averaged anisotropic correction factors (left panels) and reflected SW flux at the TOA (right panels) values when varying the ADMs TOA albedo values of $\pm 25\%$. Comparisons is presented for three of the nine study areas defined in Fig. 1. The following combination of scene types are considered: (A) ocean and bright vegetation (OC-BV), (B) bright desert and dark desert (BD-DD), and (C) bright vegetation and dark vegetation (BV-DV).

respectively). Similarly to the instantaneous errors, the largest flux differences are reported along the coastline of continents. Table IV indicates that typical errors over a set of coastal footprints in which the fraction of land varies continuously from 0% to 100% range from about 2% to 11%. Note that largest errors appear at the junction between the ocean and bright land surfaces (BV and BD) than between the ocean and dark land surfaces (DV and DD). Regarding the junctions between two different land surface types, Table IV clearly shows that systematic errors are not so conspicuous (errors ranging from about 0.1% to 1%). An exception is reported at the junction between the two desert surfaces, where a relative difference of 4.8% in the averaged flux appears for February 2003.

VI. Final Discussion and Conclusion

Because satellite radiometers do not measure the instantaneous reflected SW flux at the TOA directly, ADMs are required to relate the actual radiance measurement to flux at given solar angle, satellite-viewing geometries, and surface and atmospheric conditions. Unfortunately, while the recently developed CERES–TRMM broadband SW ADMs [12] undoubtedly represent a major advance over previous ADMs regarding the number of available ADM scene types as well as in terms of angular bins resolution, no attempt was done to derive models for mixed scene types. However, as the physical and optical properties of a scene have a strong influence on the anisotropy of the radiation at the top of the atmosphere, ignoring modifications in these properties causes TOA flux errors.

Analyzing SW flux values retrieved over various areas in the MS-7 FOV, we showed that a radiance-to-flux conversion using the ADM that corresponds to the scene type with the highest percent coverage over footprints containing a mixture of scene types can lead to generate a large flux discontinuity when shifting from one CERES–TRMM SW ADM to another. The magnitude of the flux difference depends on the surface anisotropy difference existing between the two scene types in presence. The largest flux discontinuities take place in coastal zones at the junction between oceanic and continental surface types. Our results indicate that the retrieved instantaneous SW flux at the TOA can vary up to about 32% (relative difference) when shifting from the clear-sky oceanic ADM to the bright vegetation ADM. By contrast, the shift from the bright vegetation ADM to the dark desert ADM impacted in maximum for about 0.8% on the retrieved SW flux. While reduced in regards to the instantaneous errors in the flux values retrieved over individual footprints, our results indicate that systematic errors in flux are not negligible at least over coastal areas. Averaged over a set of coastal footprints in which the fraction of land varies continuously from 0% to 100%, the magnitude of systematic errors accounts for 2% to 11% in the averaged SW flux values.

However, in the absence of available ADMs for mixed scene types, our results indicate that it is possible to combine the existing CERES–TRMM broadband SW ADMs to derive reliable mixed CERES–TRMM scene types ACFs. Computation of such factors require to approximate the reflected SW flux at the TOA over pure scene types by the corresponding ADM flux values (actually the TOA albedo). Validity of the approximation will, therefore, depend on the difference existing between the actual physical and optical properties of the surfaces contained in the footprints and the corresponding CERES–TRMM ADM scene types (possible temporal variation). Regarding the idealized situations, our results indicate that the maximum error introduced in the retrieved instantaneous SW flux due to the ADM approximation in the mixed scene types ACF computation ranges from less than 0.01% to 1.75% (relative difference). In practice, the errors will certainly be larger but negligible in regard to the ones introduced without accounting for mixed scene types ACFs.

TABLE IV
DIFFERENCES BETWEEN AVERAGED SW FLUX VALUES COMPUTED ACCORDING TO THE HIGHEST PERCENT COVERAGE ADM SCENE TYPE AND TO THE MIXED SCENE TYPES ANISOTROPIC CORRECTION FACTOR METHODS: $\bar{F} - \bar{F}_{\bar{A}_2/\bar{A}_1}$ AND $\bar{F} - \bar{F}_{\bar{F}_2/\bar{F}_1}$, RESPECTIVELY. ONLY SW FLUX VALUES RETRIEVED OVER CLEAR-SKY FOOTPRINTS CONTAINING A MIXTURE OF SCENE TYPES HAVE BEEN CONSIDERED IN THE AVERAGING PROCESS. FOR EACH STUDY AREA (DEFINED IN FIG. 1) AVERAGED FLUXES DIFFERENCES COMPUTED FROM THE 12:00 UTC MS-7 TIME SLOT ARE PROVIDED ON A DAILY (SELECTED DAY) AND MONTHLY MEAN BASIS (FEBRUARY AND JULY 2003, RESPECTIVELY). THE SAME SCENE TYPES AS IN TABLE II ARE CONSIDERED. VALUES IN BRACKETS ARE THE RELATIVE DIFFERENCES IN PERCENT

Scene types	Selected days		February 2003		July 2003	
	$\lvert\bar{F} - \bar{F}_{\bar{A}_2/\bar{A}_1}\rvert$	$\lvert\bar{F} - \bar{F}_{\bar{F}_2/\bar{F}_1}\rvert$	$\lvert\bar{F} - \bar{F}_{\bar{A}_2/\bar{A}_1}\rvert$	$\lvert\bar{F} - \bar{F}_{\bar{F}_2/\bar{F}_1}\rvert$	$\lvert\bar{F} - \bar{F}_{\bar{A}_2/\bar{A}_1}\rvert$	$\lvert\bar{F} - \bar{F}_{\bar{F}_2/\bar{F}_1}\rvert$
OC-BV	10.57 (9.5%)	10.21 (9.2%)	10.75 (9.4%)	10.39 (9.1%)	6.95 (4.5%)	7.01 (4.5%)
OC-DV	4.78 (3.6%)	3.36 (2.5%)	6.32 (4.5%)	3.88 (2.8%)	3.33 (2.8%)	5.80 (4.8%)
OC-BD	27.65 (9.7%)	20.06 (7.0%)	34.48 (11.1%)	24.05 (7.8%)	29.24 (8.4%)	23.57 (6.7%)
OC-DD	5.68 (3.9%)	6.24 (4.3%)	10.31 (6.6%)	9.66 (6.2%)	4.16(2.5%)	3.07(1.8%)
BD-DD	0.20 (0.1%)	0.52 (0.2%)	9.95 (4.8%)	9.40 (4.5%)	1.15 (0.4%)	0.47 (0.2%)
BD-BV	3.17 (1.1%)	2.79 (1.0%)	3.96 (1.4%)	3.54 (1.2%)	0.16 (0.1%)	0.59 (0.2%)
BV-DV	0.62 (0.3%)	0.43 (0.2%)	0.07 (0.03%)	0.08 (0.04%)	0.33 (0.2%)	0.29 (0.1%)
BV-DD	< 0.01	0.06 (0.03%)	0.13 (0.1%)	0.09 (0.04%)	0.02 (0.01%)	0.04 (0.02%)
DD-DV	1.12 (0.7%)	1.12 (0.7%)	1.80(1.0%)	1.80 (1.0%)	0.92 (0.5%)	0.90 (0.5%)

Approximating pure scene types SW flux values by the SW flux values retrieved over the corresponding closest (geographically speaking) pure scene types footprints allows to reduce the gap between the physical and optical properties of the surfaces contained in the footprint and the CERES–TRMM ADM scene types characteristics. Nevertheless, mixed scene types ACFs computed according to the neighboring flux approximation approach require additional computing time by comparison to the ADM flux approximation method. Moreover, the benefit related to neighboring flux approximation is largely dependent on the cloud cover. In the absence of clear-sky footprints containing only a pure scene surrounding the clear mixed scene type footprints, errors introduced by the use of SW flux retrieved over distant footprints in the ACF computation could be larger than the ones associated with the ADM flux approximation. Therefore, mixed scene types ACFs computed according to the ADM flux approximation method appear as more appropriate in the context of the GERB nearly real-time processing constraint.

Finally, as mentioned in the Introduction, CERES flux retrievals for the Terra satellite do consider mixed-scene pixels at the boundaries between land and ocean and between snowy and snow-free areas. Terra CERES pixels with mixed scene types are handled using an approach similar to the one advocated in this paper for TRMM CERES. Therefore, it is worth pointing out that our study is relevant mainly for TRMM CERES measurements.

REFERENCES

[1] V. Ramanathan, "The role of earth radiation budget studies in climate and general circulation research," *J. Geophys. Res.*, vol. 92, pp. 4075–4095, 1987.

[2] G. L. Smith, R. N. Green, E. Raschke, L. M. Avis, J. T. Suttles, B. A. Wielicki, and R. Davies, "Inversion methods for satellite studies of the Earth's radiation budget: Development of algorithms for the ERBE mission," *Rev. Geophys.*, vol. 24, no. 2, pp. 407–421, 1986.

[3] J. T. Suttles, R. N. Green, P. Minnis, G. L. Smith, W. F. Staylor, B. A. Wielicki, I. J. Walker, D. E. Young, V. R. Taylor, and L. L. Stowe, "Angular radiation models for earth–atmosphere systems," NASA, Washington, D.C., Rep. NASA RP-1184, vol. I, Short Wave Radiation, 1988.

[4] E. Raschke, T. H. Vonder Haar, W. R. Bandeen, and M. Pasternak, "The annual radiation balance of the earth–atmosphere system during 1969–1970 from Nimbus-3 measurements," *J. Atmos. Sci.*, vol. 30, no. 3, pp. 341–364, 1973.

[5] A. Gruber, "Determination of the earth–atmosphere radiation budget from NOAA satellite data," Dept. Commerce, Washington, DC, NOAA Tech. Rep. NESS 76, 1977.

[6] H. Jacobowitz, H. Soule, L. H. Kyle, and F. B. House, "The Earth Radiation Budget (ERB) Experiment: An overview," *J. Geophys. Res.*, vol. 89, no. D4, pp. 5021–5038, 1984.

[7] V. R. Taylor and L. L. Stowe, "Reflectance characteristics of uniform earth and cloud surfaces derived from Nimbus 7 ERB," *J. Geophys. Res.*, vol. 89, pp. 4987–4996, 1984.

[8] J. T. Suttles, R. N. Green, G. L. Smith, B. A. Wielicki, I. J. Walker, V. R. Taylor, and L. L. Stowe, "Angular radiation models for earth–atmosphere systems," NASA, Washington, D.C., Rep. NASA RP-1184, vol. II, Long Wave Radiation, 1988.

[9] B. R. Barkstrom, "The Earth Radiation Budget Experiment (ERBE)," *Bull. Amer. Meteorol. Soc.*, vol. 65, pp. 1170–1186, 1984.

[10] B. R. Barkstrom, E. Harrison, G. Smith, R. Green, J. Kibler, and R. Cess, "Earth Radiation Budget Experiment (ERBE) archival and April 1985 results," *Bull. Amer. Meteorol. Soc.*, vol. 70, pp. 1254–1262, 1989.

[11] B. A. Wielicki and R. N. Green, "Cloud identification for ERBE radiation flux retrieval," *J. Appl. Meteorol.*, vol. 28, pp. 1133–1146, 1989.

[12] N. G. Loeb, N. M. Smith, S. Kato, W. F. Miller, S. K. Gupta, P. Minnis, and B. A. Wielicki, "Angular distribution models for top-of-atmosphere radiative flux estimation from the clouds and the earth's radiative flux estimation from the clouds and the earth's radiant energy system instrument on the tropical rainfall measuring mission satellite. Part I: Methodology," *J. Appl. Meteorol.*, vol. 42, pp. 240–265, 2003.

[13] B. A. Wielicki, B. R. Barkstrom, E. F. Harrison, R. B. Lee, III, G. L. Smith, and J. E. Cooper, "Clouds and the Earth's Radiant Energy System (CERES): An earth observing system experiment," *Bull. Amer. Meteorol. Soc.*, vol. 77, pp. 853–868, 1996.

[14] C. Kummerow, W. Barnes, T. Kozu, J. Shiue, and J. Simpson, "The Tropical Rainfall Measuring Mission (TRMM) sensor package," *J. Atmos. Oceanic Technol.*, vol. 15, pp. 809–817, 1998.

[15] N. G. Loeb, S. Kato, and B. A. Wielicki, "Defining top-of-atmosphere flux reference level for earth radiation budget studies," *J. Clim.*, vol. 15, pp. 3301–3309, 2002.

[16] J. L. Roujean, M. Leroy, and P. Y. Deschamps, "A bidirectional reflectance model of the earth's surface for the correction of remote sensing data," *J. Geophys. Res.*, vol. 97, no. D18, pp. 20 455–20 468, 1992.

[17] J. E. Harries and D. Crommelynck, "The geostationary earth radiation budget experiment on MSG-1 and its potential applications," *Adv. Space Res.*, vol. 24, pp. 915–919, 1999.

[18] J. Schmetz, P. Pili, S. Tjemkes, D. Just, J. Kerkmann, S. Rota, and A. Ratier, "An introduction to Meteosat Second Generation (MSG)," *Bull. Amer. Meteorol. Soc.*, vol. 83, pp. 977–992, 2002.

[19] N. Clerbaux, "Meteosat count versus CERES–TRMM unfiltered radiance," RMIB, Brussels, Belgium, GERB Tech. Note MSG-RMIB-GE-TN-0036, 2002.
[20] A. S. Belward, "The IGBP-DIS global 1 km land cover data set (DISCover)—Proposal and implementation plans," IGBP-DIS , Toulouse, France, IGBP-DIS Working Paper 13, 1996.
[21] A. S. Belward, J. E. Estes, and K. D. Kline, "The IGBP-DIS 1-km land-cover data set DISCover: A project overview," *Photogramm. Eng. Remote Sens.*, vol. 65, no. 9, pp. 1013–1020, 1999.
[22] A. Ipe, C. Bertrand, N. Clerbaux, S. Dewitte, L. Gonzalez, and B. Nicula, "Validation and homogenization of the cloud properties retrievals for RMIB GERB/SEVIRI scene identification," *Proc. SPIE*, vol. 4882, pp. 29–39, 2002.
[23] A. Ipe, C. Bertrand, N. Clerbaux, S. Dewitte, and L. Gonzalez, "Validation and homogenization of cloud optical depth and cloud fraction retrievals for GERB/SEVIRI scene identification using Meteosat-7 data," *Atmos. Res.*, vol. 72, pp. 17–37, 2004.

Cédric Bertrand received the M.Sc. and Ph.D. degrees in applied natural sciences (environmental sciences) from the Université Catholique de Louvain (UCL), Louvain-la-Neuve, Belgium, in 1994 and 1998, respectively.

He was a Research Scientist with the Institut d'Astronomie et de Géophysique G. Lemaître, Department of Physics, UCL, from 1994 to 1999. During this time period, his main scientific research interests were in the field of the decadal-centennial-scale climate variability (patterns and nature of climate change and their relevance to understanding present climate change and future projections of climate change). Then, he joined the Centre d'Applications et de Recherches en Télédection of the Université de Sherbrooke, Sherbrooke, QC, Canada, for a postdoctoral position in the field of aerosol retrieval from satellite data. In September 2001, he began working on the GERB ground segment at the Remote Sensing from Space Section, Royal Meteorological Institute of Belgium, Brussels.

Nicolas Clerbaux received an engineering degree in applied physics from the Université Libre de Bruxelles, Brussels, Belgium, in 1992.

He is currently an Assistant Research Scientist in the Remote Sensing from the Space Section, Royal Meteorological Institute of Belgium, Brussels. His research interests focus on the inversion of satellite measurements for the evaluation of the earth radiation budget.

Alessandro Ipe received the M.S. degree in physics engineering and the M.S. degree in theoretical physics in 1999 from the Université Libre de Bruxelles, Brussels, Belgium, in 1998 and 1999, respectively.

He is currently a Research Assistant in the Department of Observations, Royal Meteorological Institute of Belgium (RMIB), Brussels. He is a GERB Team member responsible for the retrieval of cloud optical properties from the narrowband SEVIRI imager in the RMIB GERB ground segment processing.

Steven Dewitte received the diploma of civil engineer in electromechanics and the Ph.D. degree in applied sciences from the Vrije Universiteit Brussel (VUB), Brussels, Belgium, in 1992 and 1998, respectively. His Ph.D. thesis was on the subject of derivation of the earth radiation budget data from Meteosat images.

He is currently with the remote sensing from space group at the Royal Meteorological Institue of Belgium (RMIB), Brussels. He is a member of the GERB, CERES, ScaRaB, and VIRGO science teams, as well as a Co-Investigator for SOLCON. In 1998, he became an Assistant with the Department of Electronics, VUB. During this period, his main scientific research interests were in the field of the wavelet transform and Meteosat image processing, more specifically image compression and cloud motion detection. He currently works at RMIB on the definition and implementation of the real-time GERB ground segment software, combined with part-time lecturing in electronics at VUB.

Luis Gonzalez received the engineering degree in physics from the Université Libre de Bruxelles (ULB), Brussels, Belgium, in 1992.

After one year of research at ULB on neural networks, he worked on digital signal and image processing for real-time systems. He is currently a Research Assistant in the Department of Observations, Royal Meteorological Institute of Belgium (RMIB), Brussels, and is involved in the RMIB GERB ground segment processing.